

Take Your Steps: Hierarchically Efficient Pulmonary Disease Screening via CT Volume Compression

Qian Shao †, Kai Zhang †, Bang Du, Zepeng Li, Yixuan Wu, Qiyuan Chen, Jian Wu, *Member, IEEE*, Jintai Chen, Honghao Gao*, *Senior Member, IEEE*, Hongxia Xu*

Abstract—Deep learning models are widely used to process Computed Tomography (CT) data in the automated screening of pulmonary diseases, significantly reducing the workload of physicians. However, the three-dimensional nature of CT volumes involves an excessive number of voxels, which significantly increases the complexity of model processing. Previous screening approaches often overlook this issue, which undoubtedly reduces screening efficiency. Towards efficient and effective screening, we design a hierarchical approach to reduce the computational cost of pulmonary disease screening. The new approach reorganizes the screening workflows into three steps. First, we propose a Computed Tomography Volume Compression (CTVC) method to select a small slice subset that comprehensively represents the whole CT volume. Second, the selected CT slices are used to detect pulmonary diseases coarsely via a lightweight classification model. Third, an uncertainty measurement strategy is applied to identify samples with low diagnostic confidence, which are re-detected by radiologists. Experiments on two public pulmonary disease datasets demonstrate that our approach achieves comparable accuracy and recall while reducing

the time by 50%-70% compared with the counterparts using full CT volumes. Besides, we also found that our approach outperforms previous cutting-edge CTVC methods in retaining important indications after compression.

Index Terms—Comprehensive subset selection, Computed tomography, Pulmonary disease screening

I. INTRODUCTION

In recent years, the COVID-19 pandemic has spread globally, posing unprecedented challenges to public health systems due to its high transmissibility and severe lung impact. This pandemic has not only exposed the weaknesses in various countries' healthcare systems in responding to public health emergencies but has also created an urgent need for screening and diagnostic technologies. With the rapid advancements in medical imaging and deep learning algorithms, more researchers are utilizing deep learning methods to achieve expert-level disease screening, significantly reducing physicians' workloads [1]. CT data are extensively used for diagnosing and screening various pulmonary diseases, such as lung carcinoma and pneumonia, due to CT's ability to reveal crucial details specific to individual patients [2]. However, pulmonary CT volumes, consisting of dozens or even hundreds of individual slices, present high computational complexity and require substantial memory capacity for processing—resources that are often limited in real-world medical settings.

Previous automatic CT-based screening methods often fail to balance accuracy and efficiency. To achieve high efficiency, earlier research proposed various methods to reduce the CT slice number, thereby compressing CT volume and alleviating the dependency on extensive computational resources. These methods include CT slice selection methods [3], [4] and interpolation-based methods [5]–[7]. However, CT slice selection methods cannot guarantee that the compressed CT data can represent the entire CT volume, with a high likelihood of missing critical information. Interpolation-based methods may even introduce artefacts, as shown in Fig. 1. Intuitively, using the full CT volume for disease screening ensures relatively higher accuracy, but this approach cannot guarantee high efficiency and is, therefore, unsuitable for tasks requiring timely monitoring of infectious pulmonary diseases.

To efficiently and accurately screen for pulmonary diseases, we design a hierarchically efficient screening approach. Dif-

This research was partially supported by National Natural Science Foundation of China under grants No. 82202984, Zhejiang Key R&D Program of China under grant No. 2023C03053 and No. 2024SSYS0026.

Qian Shao is with State Key Laboratory of Transvascular Implantation Devices of The Second Affiliated Hospital, School of Medicine, and College of Computer Science & Technology, Zhejiang University, Hangzhou, China. E-mail: 12221112@zju.edu.cn.

Kai Zhang is with School of Public Health, Zhejiang University, Hangzhou, China. E-mail: zhangkai1999@zju.edu.cn.

Bang Du, Zepeng Li, and Qiyuan Chen are with College of Computer Science & Technology, Zhejiang University, Hangzhou, China. E-mails: bangdu1994@zju.edu.cn, lizepeng@zju.edu.cn, chen-qiyuan1012@foxmail.com.

Yixuan Wu is with Liangzhu Laboratory, School of Medicine, Zhejiang University, Hangzhou, China. E-mail: wyx.chloe@zju.edu.cn.

Jian Wu is with State Key Laboratory of Transvascular Implantation Devices of The Second Affiliated Hospital School of Medicine and School of Public Health, Zhejiang University, Hangzhou, China. E-mail: wujian2000@zju.edu.cn.

Jintai Chen is with Computer Science Department, University of Illinois at Urbana-Champaign. E-mail: jtchen721@gmail.com.

Honghao Gao is with College of Future Industry, Gachon University, Korea and School of Computer Engineering and Science, Shanghai University, China. E-mail: honghaogao@gachon.ac.kr; gaohonghao@shu.edu.cn.

Hongxia Xu is with Innovation Institute for Artificial Intelligence in Medicine, Zhejiang University, Hangzhou, China. E-mail: einstein@zju.edu.cn.

† These authors contributed equally to this work.

* corresponding authors.

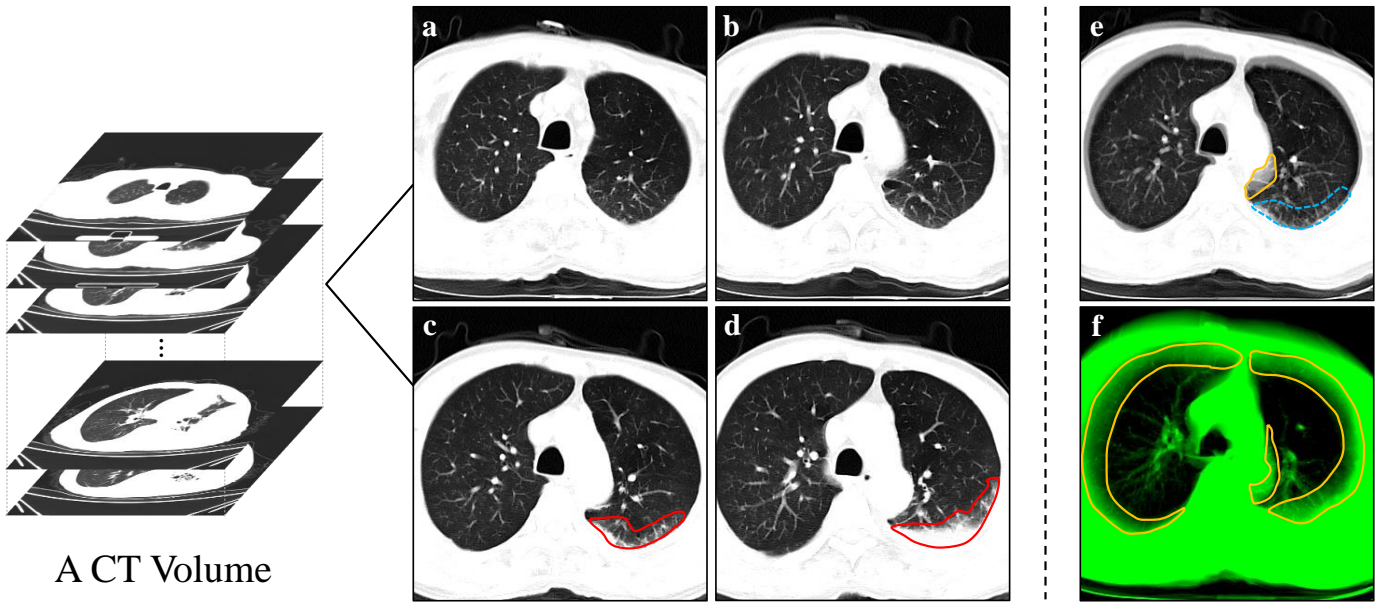


Fig. 1. Visualization results of interpolation-based methods. a-d represent four consecutive slices that contain Common Pneumonia (CP) lesions; e and f illustrate the visualization results obtained from the spline interpolation and projection interpolation, respectively. Within these visualizations, areas enclosed by red solid lines represent the CP lesions, while regions within yellow solid lines indicate artefacts generated after processing. And areas enclosed by blue dashed lines depict regions where lesions were eliminated after processing.

ferent from previous screening approaches, hierarchically efficient screening means that our method divides the screening process into two steps, namely preliminary screening and re-detection, to ensure efficiency. The core methodology insight is leveraging a Comprehensive Subset Selection (CSS) method to select representative slices for coarse detection, which means that the selected slices represent the entire CT volume, reducing the likelihood of omitting slices containing crucial indicators. Then, during the inference phase, we devise an uncertainty strategy to identify samples with low diagnostic confidence. Radiologists will re-detect these samples.

We conduct comparative experiments on two publicly available CT datasets to verify the accuracy and efficiency of our proposed screening approach, containing screening tasks for three types of pulmonary diseases, with a total of 2654 CT volumes. Specifically, we train classification networks using CT data compressed by different methods and compare their accuracy and recall. The experimental results demonstrate that our proposed CSS method significantly outperforms other methods. Furthermore, we explore the performance of the classification model under extreme conditions. For instance, when retaining only 4 slices from a single CT volume, the classification model still achieves a recall of 95.19% in the screening task for COVID-19. Based on this, we apply the uncertainty strategy to select low-confidence samples for re-detection, further improving the recall and meeting the clinical diagnosis standards. This proves that the uncertainty strategy screens out low-confidence cases that contain most of the misdiagnosed samples, which can provide a reference value for actual disease screening tasks. Finally, we compare the inference time of different methods, validating the efficiency of our approach.

In summary, the main contributions of this article are as

follows:

- 1) We design a novel hierarchical approach based on CT data for accurate and efficient screening of pulmonary diseases.
- 2) We propose a slice selection method CSS, which can select a representative slice subset from the whole CT volume, thereby enabling efficient screening.
- 3) We adopt an uncertainty strategy to select low-confidence samples for re-detection during the inference phase, ensuring the accuracy of the screening.
- 4) We validate the efficiency and accuracy of our proposed screening system on two public CT datasets. Experiments show that our screening method can achieve similar performance while reducing the time by 50%–70% compared with the method using full CT volumes.

II. RELATED WORK

A. Pulmonary Disease Screening

With the development of deep learning, more and more studies have used deep learning to achieve automatic screening of pulmonary diseases, which greatly reduces the workload of clinicians. These studies usually utilize X-ray images or CT volumes to detect pulmonary diseases. For example, Dhaka *et al.* develop a convolutional neural network (CNN) named COVID-Screen-Net for screening of COVID-19 using chest X-ray images [1]. Iqbal *et al.* propose a deep learning-based framework TBXNet for tuberculosis detection using X-ray images [8]. Schroeder *et al.* design a CNN to predict chronic obstructive pulmonary disease using chest X-ray images and Pulmonary Function Test (PFT) exams [9]. Harsono *et al.* propose a novel lung nodule detection and classification model called I3DR-Net using thorax CT scans [10]. Agarwala *et al.* develop a deep-learning method for the detection of interstitial

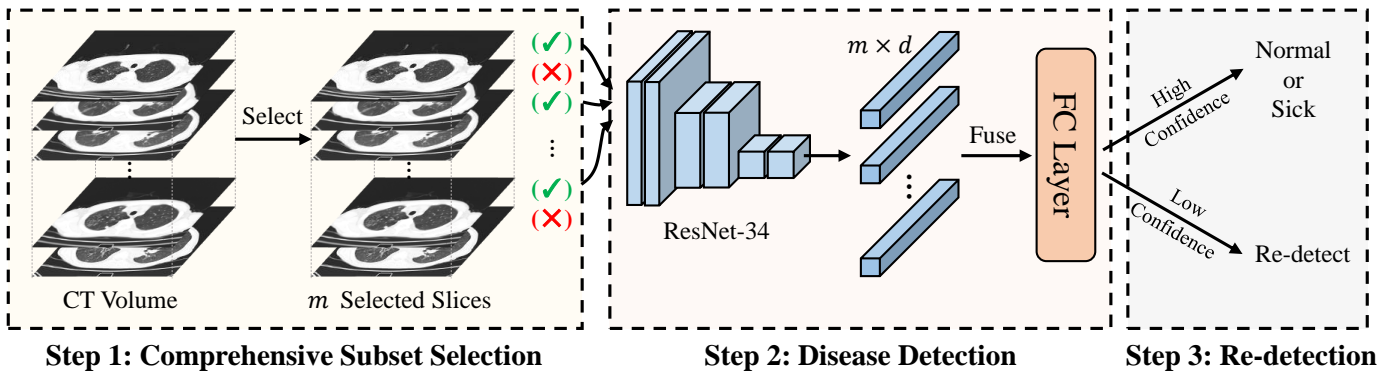


Fig. 2. The overall process of our proposed screening approach.

lung disease patterns using high-resolution CT images [11]. Ardila *et al.* propose an end-to-end lung cancer screening method with three-dimensional deep learning using low-dose chest CT [12]. CT scans can provide highly detailed and high-resolution images, revealing subtle anatomical structures. They can also be reconstructed into three-dimensional images by computers, offering additional information to aid diagnosis. Consequently, CT scans are more suitable for the detection and evaluation of complex diseases. Due to their three-dimensional nature, CT images typically consist of a large number of slices. When utilizing deep learning techniques for disease screening, processing CT data requires substantial computational resources. Previous studies have predominantly focused on improving screening accuracy and recall, often neglecting efficiency issues. To address this issue, we design a hierarchically efficient method for pulmonary disease screening.

B. CT Compression

Previous researches divide CT volumes into smaller patches for processing [13] to reduce the demand for large memory, which is similar to serializing parallel tasks. While they prolong the inference time, resulting in inefficiency. Recent studies have proposed various methods to process CT volumes for efficient screening of pulmonary diseases, which can be broadly categorized into two types:

1) *Slice selection-based methods*: These methods select a subset of slices from the CT volume evenly to construct the desired volume. For instance, Zunaiar *et al.* adopt Subset Slice Selection (SSS) [3] and Even Slice Selection (ESS) [4] to select a slice subset from the whole CT volume. SSS selects equal slices from the first, middle and last position of the CT volume, whereas ESS selects one after every specific number of slices. However, these approaches lack assurance that the selected slices represent the entire CT volume, as there is a high likelihood of omitting slices containing crucial indicators of the disease, leading to inaccurate screening results.

2) *Interpolation-based methods*: These methods adjust the Z-axis by either compressing or expanding it to reach the desired depth, such as Linear Interpolation (LI) [5], [14], Spline Interpolation (SI) [6], [15], [16], or Projection Interpolation (PI) [7]. However, these methods may distort the original pixel values, potentially introducing artefacts or losing lesion information, inevitably affecting screening accuracy.

C. Uncertainty Strategy

Uncertainty strategy is widely used in Active Learning (AL) methods, which aims to optimize the learning process by selecting the appropriate samples for labelling, reducing reliance on large labelled datasets. Uncertainty strategies are designed to select samples about which the current model is most uncertain. Earlier studies utilized posterior probability [17], [18], entropy [19]–[21], and classification margin [22] to estimate uncertainty. Wang *et al.* discover a large amount of high-confidence samples from the unlabeled set for feature learning, which is different from traditional methods focusing on only the uncertain samples of low prediction confidence [18]. Luo *et al.* operate with weakly labelled data and query additional examples based on entropies of local marginals, which are a good surrogate for uncertainty [20]. Tong *et al.* arrive at three algorithms that attempt to reduce version space as much as possible at each query by taking advantage of the duality between parameter space and feature space [22].

Recent research regards uncertainty as training loss [23], [24], influence on model performance [25], [26] or the prediction discrepancies between multiple classifiers [27]. Huang *et al.* design a metric named Temporal Output Discrepancy that estimates the sample loss by evaluating the discrepancy of outputs given by models at different optimization steps, inspired by the fact that the samples with higher loss are usually more informative to the model than the samples with lower loss [23]. Liu *et al.* propose the Influence Selection for Active Learning (ISAL), which selects the unlabeled samples that can provide the most positive influence on model performance [26]. Cho *et al.* propose a novel method to leverage the classifier discrepancies for the acquisition function for active learning [27].

III. METHODOLOGY

The overall process of our screening approach is divided into three steps, as shown in Fig. 2: First, we design CSS to select a slice subset that represents the entire CT volume. Second, we train a classification network to detect disease using the selected slices. Third, we adopt the uncertainty strategy to select low-confidence samples for re-detection.

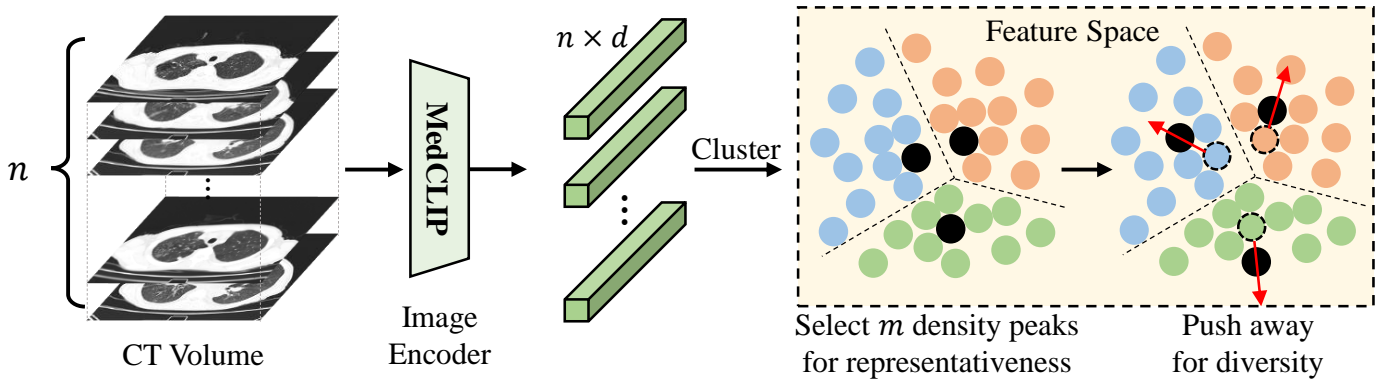


Fig. 3. The procedure of CSS. The dark circles represent the selected slices.

A. Comprehensive Subset Selection

Assuming that each CT volume contains n slices (denoted as $\{\mathbf{x}_i\}_{i=1}^n$), our goal is to select $m (\ll n)$ slices that could represent the whole CT volume so that the performance of a model trained on the selected slice subsets approaches that on the whole CT volumes. The procedure of CSS is shown in Fig. 3.

1) *Representation Learning*: We leverage the pre-trained image feature extraction capabilities of MedCLIP-ViT [28] to obtain semantically meaningful representations containing key indicators. The image encoder of MedCLIP-ViT maps \mathbf{x}_i onto a d -dimensional hypersphere with L^2 normalization, denoted as $\mathbf{f}_i = f(\mathbf{x}_i)$. Specifically, the [CLS] token features produced by the model's final output with L^2 normalization are employed for slice selection.

2) *Slice Selection*: We select CT slices according to two strategies that are representativeness and diversity [29]–[31]. The former ensures that the selected slice subset can represent the whole CT volume containing key indicators. The latter minimizes the internal similarity of the selected subset to avoid redundancy, which provides the possibility of extremely compressing the CT volume.

First, we adopt K -Means clustering that partitions n instances (*i.e.*, the CT slices in the feature space, denoted as $\{\mathbf{f}_i\}_{i=1}^n$) into $m (\leq n)$ clusters, with each cluster represented by its centroid \mathbf{c} and every instance assigned to the cluster of the nearest centroid [32], [33]. Formally, we aim to find m -cluster partitioning $\mathbb{S} = \{S_1, S_2, \dots, S_m\}$ that minimizes the within-cluster sum of squares [34]:

$$\min_{\mathbb{S}} \sum_{i=1}^m \sum_{\mathbf{f} \in S_i} \|\mathbf{f} - \mathbf{c}_i\|^2 = \min_{\mathbb{S}} \sum_{i=1}^m |S_i| \text{Var}(S_i). \quad (1)$$

It is optimized iteratively with EM [35] from random initial centroids.

Then, we select the density peaks within each cluster as the most representative slices since the density peaks are similar to as many instances as possible. The density is estimated by K -Nearest Neighbor (K -NN) [36] which is formulated as

$$\text{Den}(\mathbf{f}_i, k) = \frac{k}{n A_d \cdot D(\mathbf{f}_i, \mathbf{f}_i^k)}, \quad (2)$$

where $A_d = \pi^{d/2} / \Gamma(\frac{d}{2} + 1)$ is the volume of a unit d -dimensional ball, d is the feature dimension, $\Gamma(x)$ is the

Gamma function, and $D(\mathbf{f}_i, \mathbf{f}_i^k) = \|\mathbf{f}_i - \mathbf{f}_i^k\|$ is the feature distance between two instances, \mathbf{f}_i^k is the k th nearest neighbor of \mathbf{f}_i . Intuitively, the smaller the feature distance, the greater the similarity of the instances. However, $\text{Den}(\cdot, \cdot)$ is very sensitive to noise, as it only takes the k th nearest neighbour into account. For robustness, we replace the k th neighbor distance $D(\mathbf{f}_i, \mathbf{f}_i^k)$ with the average distance $\bar{D}(\mathbf{f}_i, k)$ to all k nearest neighbors instead:

$$\hat{\text{Den}}(\mathbf{f}_i, k) = \frac{k}{n A_d \cdot \bar{D}(\mathbf{f}_i, k)}, \quad (3)$$

where $\bar{D}(\mathbf{f}_i, k) = \frac{1}{k} \sum_{j=1}^k D(\mathbf{f}_i, \mathbf{f}_i^j)$. To sum up, $\hat{\text{Den}}(\mathbf{f}_i, k)$ is used to measure the representativeness of instance \mathbf{f}_i . Since only the relative ordering matters in our selection process, the density peak corresponds to the instance with maximum $\hat{\text{Den}}(\mathbf{f}_i, k)$, *i.e.*, minimum $\bar{D}(\mathbf{f}_i, k)$.

However, when the clustering boundaries are located in high-density areas, the selected instances may align along these boundaries and become proximal to each other, leading to redundancy. Therefore, we apply a regularizer to diversify the selected instances in the feature space iteratively. In detail, let $\hat{\mathbb{F}}^t = \{\hat{\mathbf{f}}_1^t, \hat{\mathbf{f}}_2^t, \dots, \hat{\mathbf{f}}_m^t\}$ denote the set of m instances selected at iteration t , $\hat{\mathbf{f}}_i^t$ is selected from clusters S_i , where $i \in \{1, 2, \dots, m\}$. For each candidate \mathbf{f}_i in cluster S_i , the farther it is away from those in other clusters in $\hat{\mathbb{F}}^{t-1}$, the more diversity it creates. We thus minimize the total inverse distance to others in a regularization loss $\text{Reg}(\mathbf{f}_i, t)$, with a sensitivity hyperparameter α :

$$\text{Reg}(\mathbf{f}_i, t) = \sum_{j \neq i} \frac{1}{\|\mathbf{f}_i - \hat{\mathbf{f}}_j^{t-1}\|^\alpha}. \quad (4)$$

This regularizer is updated with an exponential moving average [37]:

$$\overline{\text{Reg}}(\mathbf{f}_i, t) = m_{\text{reg}} \cdot \overline{\text{Reg}}(\mathbf{f}_i, t-1) + (1 - m_{\text{reg}}) \cdot \text{Reg}(\mathbf{f}_i, t), \quad (5)$$

where m_{reg} is the momentum. At iteration t , we select instance i of the maximum combination of representativeness and diversity $C(\mathbf{f}_i, t)$ within each cluster:

$$C(\mathbf{f}_i, t) = \frac{1}{\bar{D}(\mathbf{f}_i, k)} - \lambda \cdot \overline{\text{Reg}}(\mathbf{f}_i, t), \quad (6)$$

where λ is a hyperparameter that balances diversity and representativeness. At the last iteration, the instances in $\hat{\mathbb{F}}$ are the selected CT slices for the downstream task.

We present the slice selection algorithm in pseudo-code form, as shown in Alg. 1. In Alg. 1, we first obtain $\hat{\mathbb{F}}^0$, which is the initial selection without regularization, and set the moving average regularization item $\overline{\text{Reg}}(\mathbf{f}_i, 0)$ to 0 for every $\mathbf{f}_i \in \mathbb{F}$. Then, in each iteration, we update $\overline{\text{Reg}}(\mathbf{f}_i, t)$ with moving average from a distance measurement to other instances selected in the previous iteration, where t represents the current iteration. We re-select samples according to the regularization item at the end of each iteration with a trade-off parameter λ . The selected instances in the last iteration are returned.

Algorithm 1 Pseudo-code for Slice Selection Algorithm.

INPUT:

$\{\overline{D}(\mathbf{f}_i, k) | \mathbf{f}_i \in \mathbb{F}\}$: average distance to all k nearest neighbors of each \mathbf{f}_i ;

λ : weight for applying regularization;

m_{reg} : momentum in exponential moving average;

T : the number of iterations.

OUTPUT:

$\hat{\mathbb{F}}^T$: the selected instances after T iterations.

PROCEDURE:

$\overline{\text{Reg}}(\mathbf{f}_i, 0) \leftarrow 0, \forall \mathbf{f}_i \in \mathbb{F}$

$\hat{\mathbb{F}}^0 \leftarrow$ instances with largest $\frac{1}{\overline{D}(\mathbf{f}_i, k)}$ in each cluster

for $t = 1$ **to** T **do**

for all $\mathbf{f}_i \in \mathbb{F}$ **do**

$\text{Reg}(\mathbf{f}_i, t) \leftarrow \sum_{j \neq i} \frac{1}{\|\mathbf{f}_i - \hat{\mathbf{f}}_j^{t-1}\|^\alpha}$

$\overline{\text{Reg}}(\mathbf{f}_i, t) \leftarrow m_{\text{reg}} \cdot \overline{\text{Reg}}(\mathbf{f}_i, t-1) + (1 - m_{\text{reg}}) \cdot$

$\text{Reg}(\mathbf{f}_i, t)$

$C(\mathbf{f}_i, t) \leftarrow \frac{1}{\overline{D}(\mathbf{f}_i, k)} - \lambda \cdot \overline{\text{Reg}}(\mathbf{f}_i, t)$

end for

$\hat{\mathbb{F}}^t \leftarrow$ instances with largest $C(\mathbf{f}_i, t)$ in each cluster

end for

return $\hat{\mathbb{F}}^T$

B. Disease Detection

We train a classification model using the selected slices for disease detection. First, ResNet-34 [38] is used to extract image features of m slices in each case, denoted as $f_{\text{Res}}(\mathbf{x}_i)$, where $i \in \{1, 2, \dots, m\}$. Details of ResNet-34 are as follows: the $1000 - d$ Fully-Connected (FC) layer in the penultimate layer is replaced with a $512 - d$ FC layer, and the last SoftMax layer is deleted. Then, the output of ResNet-34 is used as input to a light transformer-based network [39] for feature fusion, where both the layer number and the head number of the Transformer Encoder are set to 6. Finally, we perform an FC layer and Softmax on the output of the transformer-based network to predict the probability of disease. The prediction loss function is a cross-entropy loss function, which can be expressed as:

$$\text{Loss} = -\frac{1}{B} \sum_{j=1}^B \sum_{i=1}^M y_{ji} \log(\hat{y}_{ji}), \quad (7)$$

where B is the batch size, M is the number of classes, y_{ji} is the real probability that the j -th sample belongs to i -th

category, and \hat{y}_{ji} is the predicted probability that the j -th sample belongs to i -th category.

C. Low-confidence Case Re-detection

We select B most uncertain cases as low-confidence ones which will be re-detected using their corresponding full CT volumes by radiologists. Specifically, the uncertainty is measured by the entropy criteria [21], which is defined as

$$en_i = -\sum_{j=1}^M p(y_i = j | c_i; \theta) \log p(y_i = j | c_i; \theta), \quad (8)$$

where en_i is the entropy of i th case c_i , $p(y_i = j | c_i; \theta)$ denotes the probability of c_i belonging to the j th class. M is the number of classes and θ represent the parameters of the classification model described in Section III-B. Entropy takes all class label probabilities into consideration to evaluate the uncertainty. The higher the entropy value, the more uncertain the case. We rank all the cases for detection in descending order according to their entropy values and select the first B cases as the low-confidence ones. Here, we set B to 10. Although this step reduces some screening efficiency, it significantly improves accuracy in meeting clinical requirements.

IV. EXPERIMENTS

A. Dataset

We conduct comparative experiments on two publicly available datasets: SARS-CoV-2 dataset [40] and LUNG-PET-CT-Dx [41], which are obtained from the China Consortium of Chest CT Image Investigation (CC-CCII) and The Cancer Imaging Archive (TCIA) [42], respectively. All the above datasets belong to public databases. The patients involved in the database have obtained ethical approval. Users can download relevant data for free for research and publish relevant articles. Our study is based on open source data, so there are no ethical issues and other conflicts of interest.

Given our objective to compress CT volumes, we eliminated cases with a relatively low number of slices, specifically those with less than 64 slices. After that, 2654 cases are included in the study, containing 311 cases diagnosed with adenocarcinoma (AC), 747 cases with Novel Coronavirus Pneumonia (NCP, *i.e.*, COVID-19), 741 cases with Common Pneumonia (CP) and 855 normal cases. Here, a case refers to a 3D CT volume. The AC cases are from LUNG-PET-CT-Dx, while the NCP, CP and normal cases are from the SARS-CoV-2 dataset. Then, we design three binary classification tasks to detect the above three diseases. Specifically, Task 1 contains 747 NCP and 855 normal cases; Task 2 contains 741 CP and 855 normal cases; Task 3 contains 311 AC and 311 normal cases. The normal cases for Task 3 are randomly chosen from 855 normal cases of the SARS-CoV-2 dataset. Finally, we evenly divide the dataset into 5 parts and use 5-fold cross-validation to evaluate the accuracy and recall for each task.

TABLE I

COMPARISON WITH OTHER METHODS. THE BEST PERFORMANCE IS BOLD, AND THE SECOND BEST PERFORMANCE IS UNDERLINED EXCEPT FOR THE METHOD OF FULL CT VOLUME. EACH RESULT SHOWS MEAN ACCURACY AND STANDARD DEVIATION OVER 5-FOLD CROSS-VALIDATION.

Method	Task 1		Task 2		Task 3	
	Accuracy	Recall	Accuracy	Recall	Accuracy	Recall
Full CT	99.12 \pm 0.31	99.15 \pm 0.35	99.35 \pm 0.41	99.30 \pm 0.38	92.47 \pm 0.60	92.10 \pm 0.65
PI [7]	90.36 \pm 0.34	89.02 \pm 0.41	88.92 \pm 0.40	89.00 \pm 0.30	84.59 \pm 0.47	83.50 \pm 0.52
LI [14]	78.52 \pm 2.54	77.89 \pm 2.67	73.67 \pm 2.03	71.70 \pm 2.30	68.81 \pm 3.80	67.54 \pm 4.81
SI [15]	<u>98.78\pm0.34</u>	<u>98.20\pm0.37</u>	<u>98.33\pm0.42</u>	<u>98.30\pm0.40</u>	87.24 \pm 0.40	86.94 \pm 0.37
SSS [3]	96.89 \pm 0.56	96.28 \pm 0.62	95.23 \pm 0.97	95.12 \pm 0.99	<u>89.34\pm0.90</u>	<u>89.67\pm1.24</u>
ESS [4]	96.42 \pm 0.86	96.85 \pm 0.78	94.29 \pm 1.37	94.50 \pm 1.70	<u>88.56\pm1.56</u>	<u>86.78\pm1.65</u>
CSS (Ours)	98.89\pm0.17	99.05\pm0.18	98.65\pm0.23	98.82\pm0.29	91.88\pm0.43	90.85\pm0.54

TABLE II

COMPARISON UNDER EXTREME COMPRESSION. THE BEST PERFORMANCE UNDER DIFFERENT COMPRESSION LEVELS IS BOLD. THE NUMBER AFTER THE ARROW REPRESENTS THE PERCENTAGE OF PERFORMANCE IMPROVEMENT COMPARED WITH SI METHOD.

Number	Method	Task 1		Task 2		Task 3	
		Accuracy	Recall	Accuracy	Recall	Accuracy	Recall
32	SI	97.99	98.06	96.73	97.10	83.63	83.49
	CSS	98.12 (\uparrow 0.13)	98.19 (\uparrow 0.13)	97.89 (\uparrow 1.16)	97.74 (\uparrow 0.64)	90.01 (\uparrow 6.38)	90.27 (\uparrow 6.78)
16	SI	96.99	97.21	93.87	94.07	76.71	76.90
	CSS	97.26 (\uparrow 0.27)	97.58 (\uparrow 0.37)	94.00 (\uparrow 0.13)	94.28 (\uparrow 0.21)	85.60 (\uparrow 8.89)	85.54 (\uparrow 9.64)
8	SI	95.96	95.88	92.09	92.55	67.34	67.68
	CSS	96.57 (\uparrow 0.61)	96.89 (\uparrow 1.01)	93.21 (\uparrow 1.12)	93.02 (\uparrow 0.47)	82.55 (\uparrow 15.21)	82.63 (\uparrow 14.95)
4	SI	93.86	94.24	90.03	90.78	64.41	64.57
	CSS	94.90 (\uparrow 1.04)	95.19 (\uparrow 0.95)	91.17 (\uparrow 1.14)	91.76 (\uparrow 0.98)	78.64 (\uparrow 14.23)	78.89 (\uparrow 14.32)
Full CT		99.12	99.15	99.35	99.30	92.47	92.10

B. Experimental Settings

All models are implemented in PyTorch and trained on an RTX 4090 with 24 GB memory. Considering the anatomical structure of the lungs—where the left lung is divided into upper and lower lobes with a volume ratio of approximately 0.4 : 0.6, and the right lung into upper, middle, and lower lobes with a volume ratio of approximately 0.25 : 0.15 : 0.6, we divide the entire CT volume into three distinct parts based on the ratios of 0.25 : 0.15 : 0.6. Assuming that a CT volume contains n slices, the first $0.25n$ slices are the first part after division, the middle $0.15n$ slices are the second part, and the last $0.6n$ slices are the third part. Following this, the total budget of slice selection m is distributed across these parts in accordance with the same proportion. CSS is used to select a slice subset in each part. In the process of the subset selection, we set the hyperparameters $k = 10$, $\alpha = 0.5$, $m_{\text{reg}} = 0.9$, $\lambda = 0.5$ and $t = 10$.

During the training stage of the diagnostic model, we use adaptive moment estimation (Adam) with an initial learning rate $1e^{-3}$ to optimize the network. We set different batch sizes for experiments with different numbers of compressed selected slices. The more slices selected for each case, the more GPU memory each case occupies; thus, the batch size should be smaller. In detail, $batchsize = 1, 4, 8, 16, 16$ is set for $m = 64, 32, 16, 8, 4$ respectively. For a fair comparison, the training epoch of all experiments is set to 400.

C. Comparison with Other Compression Methods

In three diagnostic tasks, we compare the performance of diagnostic models when applied with different compression methods, including three interpolation-based methods: Projection Interpolation (PI) [7], Linear Interpolation (LI) [14] and Spline Interpolation (SI) [15], two slice selection-based methods: Subset Slice Selection (SSS) [3] and Even Slice Selection (ESS) [4], and full CT volume method. Interpolation-based methods calculate the new pixel value in the compressed image based on the values of surrounding pixels on the Z-axis. As for the slice selection-based method, SSS selects equal slices from the first, middle and last position of the CT volume, whereas ESS selects one after every specific number of slices. As a baseline method, the full CT volume method utilizes the whole CT dataset for training the classification model without compression. It is worth noting that the full CT method uses 3D-ResNet [43] as the classification model.

To ensure a fair comparison, we set the number of slices after compression to 64 for each method. The experimental results are shown in Table I, from which we have several observations: (1) The performance of our method generally surpasses that of other compression methods, and it achieves performance levels very close to those of the full CT volume method across three tasks; (2) On Tasks 1 and 2, the performance of the second-best SI method is comparable to that of our method. On task 3, only our method achieves accuracy and recall above 90%. This may be attributed to the fact that Tasks 1 and 2 involve diagnosing pneumonia, where the lesion areas are larger and more distinct, thus

TABLE III

COMPARISON BEFORE AND AFTER RE-DETECTION USING UNCERTAINTY STRATEGY. THE NUMBER AFTER THE ARROW REPRESENTS THE PERCENTAGE OF PERFORMANCE IMPROVEMENT AFTER RE-DETECTION.

Task	Number	Re-detection	Accuracy	Recall
Task 1	8	Before	96.57	96.89
		After	97.24 (↑ 0.67)	97.88 (↑ 0.99)
Task 1	4	Before	94.90	95.19
		After	96.06 (↑ 1.16)	96.41 (↑ 1.22)
Task 2	8	Before	93.21	93.02
		After	94.27 (↑ 1.06)	94.59 (↑ 1.57)
Task 2	4	Before	91.17	91.76
		After	93.04 (↑ 1.87)	93.18 (↑ 1.42)
Task 3	8	Before	82.55	82.63
		After	88.53 (↑ 5.98)	88.80 (↑ 6.17)
Task 3	4	Before	78.64	78.89
		After	82.77 (↑ 4.13)	83.03 (↑ 4.14)

TABLE IV

INFERENCE TIME UNDER DIFFERENT COMPRESSION RATIOS. THE TIME SHOWN IN THE TABLE IS THE INFERENCE TIME FOR 50 CASES. THE PERCENTAGE IN BRACKETS REPRESENTS THE RATIO OF THE TIME CONSUMED BY THE CURRENT EXPERIMENT TO THE TIME CONSUMED BY THE FULL CT METHOD.

Method	Number	Task 1	Task 2	Task 3
CSS	32	77.64s (45.88%)	81.88s (43.31%)	79.53s (44.37%)
	16	59.24s (35.00%)	64.73s (34.24%)	61.65s (34.39%)
	8	50.22s (29.67%)	54.16s (28.65%)	52.34s (29.20%)
	4	45.45s (26.86%)	50.54s (26.73%)	47.38s (26.43%)
Full CT		169.24s	189.05s	179.25s

easier to differentiate from normal cases. In contrast, Task 3 focuses on detecting adenocarcinoma, where the lesion areas are smaller and morphologically complex, making accurate detection challenging. The superior performance on difficult tasks demonstrates the superiority of our method.

D. Exploration Under Extreme Compression

We explore the accuracy and recall of the diagnostic model applied with CSS under extreme compression, that is, selecting 32, 16, 8, and 4 CT slices from each case. We compare CSS not only with the full CT volume method but also with the second-best performing method described in Section IV-C, *i.e.*, SI method [15]. The experimental results are shown in Table II, from which we have several observations: (1) On Tasks 1 and 2, the performance of models applied with two compression methods is similar, while on Task 3, our method shows a significant improvement over the SI method. This conclusion aligns with the second point discussed in Section IV-C; (2) On Task 3, as the number of target slices after compression decreases, the performance improvement of our method becomes increasingly significant compared to the SI method. For instance, at $Number = 32$ and 4, the recall increased by 6.78% and 14.32%, respectively, demonstrating that under extreme compression scenarios, our method holds a greater advantage over other methods.

E. Comparison Before and After Re-detection

When selecting 8 and 4 CT slices, we verify the effectiveness of the uncertainty strategy by comparing the per-

formance before and after the re-detection. We assume all low-confidence cases will be correctly diagnosed during the re-detection phase. The experimental results are shown in Table III, from which we observe that the accuracy and recall improve after using the uncertainty strategy to filter out cases for re-detection. In particular, on Task 3, recall improves by 6.17% and 4.14% when retaining 8 and 4 slices, respectively. This proves that low-confidence cases do contain most of the misdiagnosed cases, which can provide a reference value for actual disease screening tasks.

F. Efficiency Evaluation

We evaluate the efficiency of our proposed method and the full CT method by computing the inference time while ensuring the same memory usage. The inference time of our method includes the time for feature extraction using the pre-trained model MedCLIP-ViT, the time for CSS to select representative slices, and the time to detect the disease by the classification model. The inference time of two methods under different compression rates is shown in Table IV, from which we can see that our method can reduce the inference time by more than 70% compared with the full CT method when retaining 4 slices per CT volume. Combined with the experimental results in Table II, we can reserve different numbers of CT slices for different disease diagnosis tasks in real medical scenarios. For example, if we hope to achieve an accuracy and recall rate of more than 90%, we can reserve 4, 4 and 32 slices for each case in Task 1, Task 2 and Task 3,

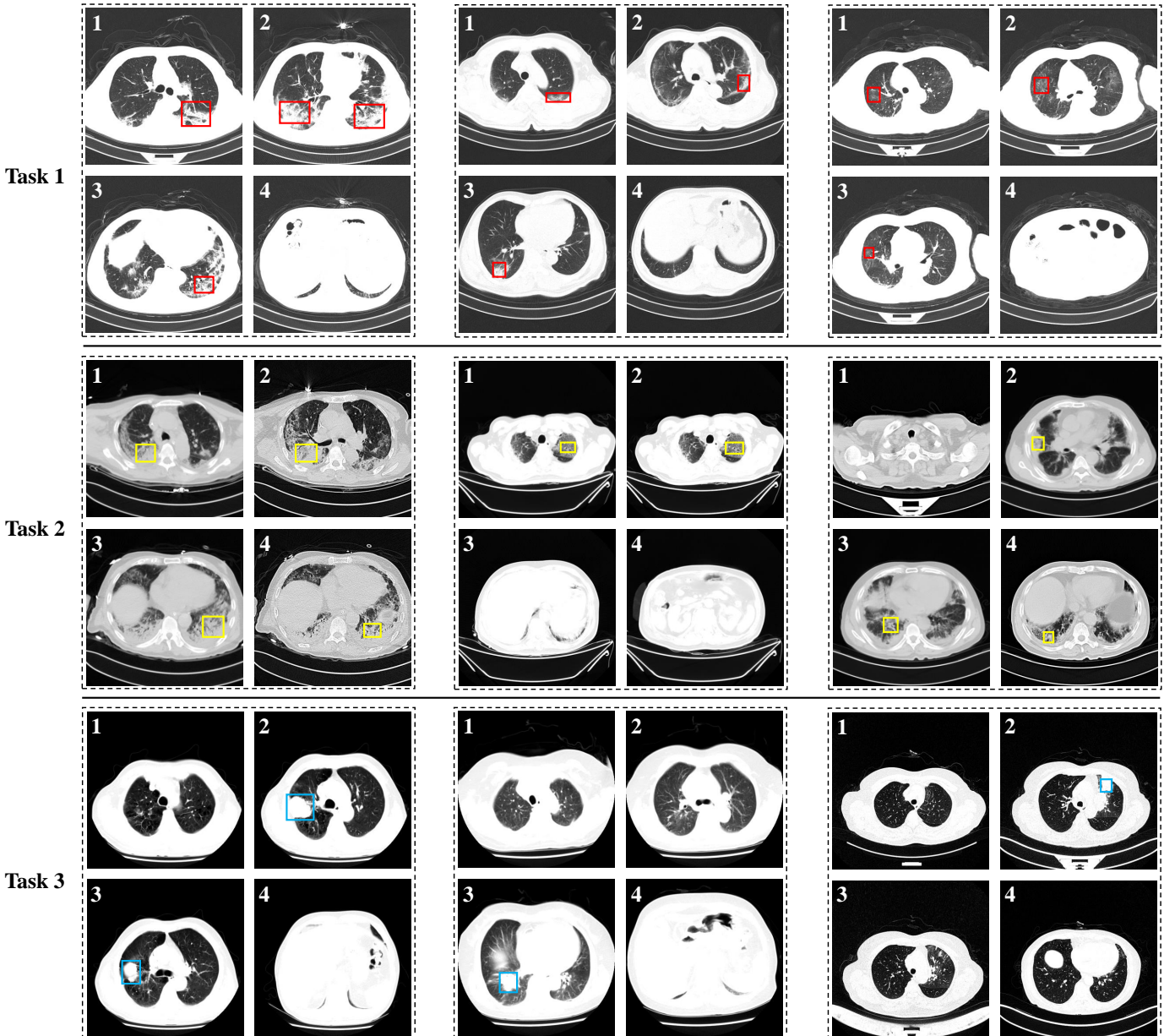


Fig. 4. Visualization of CT slices selected by our proposed CSS. The red, yellow and blue boxes mark the lesion areas of NCP, CP and AC, respectively.

respectively. Compared with the full CT method, our screening method can reduce the time by 50% – 70%.

G. Visualization

We visualize the slices selected by our proposed CSS method, as shown in Fig. 4. In Fig. 4, rows 1, 2, and 3 show the selected CT slices in Task 1, 2 and 3, respectively. Each task displays three cases, with each case retaining four slices. From Fig. 4, we have several observations: (1) the slices selected by our proposed CSS contain lesion areas, indicating that the CSS method can select representative slices to aid in diagnosis; (2) In Task 1 and Task 2, the number of slices with lesions is significantly greater than that in Task 3. For example, in Task 3, only one slice in the second and third cases has AC. This shows that in the entire CT volume, the number of slices

indicating AC may be less than those indicating pneumonia. In other words, AC is less obvious on CT and more difficult to diagnose, which is consistent with the experimental results in Section IV-C.

V. LIMITATIONS

We use representative slices selected from the entire CT volume to diagnose diseases. Although this approach reduces computational load and lowers hardware requirements, it relies solely on the information within the 2D CT slices, potentially losing spatial correlations and complete lesion structure information between slices, such as the size, shape, and location of tumours. Therefore, our proposed compressed CT method is suitable for simpler diagnostic tasks, like preliminary disease

screening, but is less suitable for complex diagnostic tasks, like cancer staging.

VI. CONCLUSIONS

In this paper, we propose a novel hierarchical approach based on CT data for accurate and efficient screening of pulmonary diseases. The core insight is leveraging a CTVC method CSS to select representative slices from full CT volumes for coarse detection. During the inference phase, we adopt an uncertainty strategy to identify cases with low diagnostic confidence, which can be referred to radiologists for re-detection in clinical practice. Extensive experimental results show that our approach achieves comparable performance while saving time by 50% – 70% when compared with the counterparts which process full CT volumes. Besides, we also found that our approach outperforms previous SOTA CTVC methods in retaining crucial information after compression.

ACKNOWLEDGMENT

We wish to thank the timely help given by Yiqun Fan in analyzing the selected CT slices in the visualization experiments.

REFERENCES

- [1] V. S. Dhaka, G. Rani, M. G. Oza, T. Sharma, and A. Misra, "A deep learning model for mass screening of covid-19," *International journal of imaging systems and technology*, vol. 31, no. 2, pp. 483–498, 2021.
- [2] A. Lewis, E. Mahmoodi, Y. Zhou, M. Coffee, and E. Sizikova, "Improving tuberculosis (tb) prediction using synthetically generated computed tomography (ct) images," in *Proceedings of the IEEE/CVF international conference on computer vision*, 2021, pp. 3265–3273.
- [3] H. Zunair, A. Rahman, and N. Mohammed, "Estimating severity from ct scans of tuberculosis patients using 3d convolutional nets and slice selection?" 2019.
- [4] H. Zunair, A. Rahman, N. Mohammed, and J. P. Cohen, "Uniformizing techniques to process ct scans with 3d cnns for tuberculosis prediction," in *Predictive Intelligence in Medicine: Third International Workshop, PRIME 2020, Held in Conjunction with MICCAI 2020, Lima, Peru, October 8, 2020, Proceedings 3*. Springer, 2020, pp. 156–168.
- [5] Q. Shao, R. Xuan, Y. Wang, J. Xu, M. Ouyang, C. Yin, and W. Jin, "Deep learning and radiomics analysis for prediction of placenta invasion based on t2wi," *Mathematical Biosciences and Engineering*, vol. 18, no. 5, pp. 6198–6215, 2021.
- [6] D. Han, Y. Chen, X. Li, W. Li, X. Zhang, T. He, Y. Yu, Y. Dou, H. Duan, and N. Yu, "Development and validation of a 3d-convolutional neural network model based on chest ct for differentiating active pulmonary tuberculosis from community-acquired pneumonia," *La radiologia medica*, vol. 128, no. 1, pp. 68–80, 2023.
- [7] V. Liauchuk, "Imageclef 2019: Projection-based ct image analysis for tb severity scoring and ct report generation." 2019.
- [8] A. Iqbal, M. Usman, and Z. Ahmed, "An efficient deep learning-based framework for tuberculosis detection using chest x-ray images," *Tuberculosis*, vol. 136, p. 102234, 2022.
- [9] J. D. Schroeder, R. Bigolin Lanfredi, T. Li, J. Chan, C. Vachet, R. Paine III, V. Srikanth, and T. Tasdizen, "Prediction of obstructive lung disease from chest radiographs via deep learning trained on pulmonary function data," *International Journal of Chronic Obstructive Pulmonary Disease*, pp. 3455–3466, 2020.
- [10] I. W. Harsono, S. Liawati, and T. W. Cenggoro, "Lung nodule detection and classification from thorax ct-scan using retinanet with transfer learning," *Journal of King Saud University-Computer and Information Sciences*, vol. 34, no. 3, pp. 567–577, 2022.
- [11] S. Agarwala, M. Kale, D. Kumar, R. Swaroop, A. Kumar, A. K. Dhara, S. B. Thakur, A. Sadhu, and D. Nandi, "Deep learning for screening of interstitial lung disease patterns in high-resolution ct images," *Clinical radiology*, vol. 75, no. 6, pp. 481–e1, 2020.
- [12] D. Ardila, A. P. Kiraly, S. Bharadwaj, B. Choi, J. J. Reicher, L. Peng, D. Tse, M. Etmedi, W. Ye, G. Corrado *et al.*, "End-to-end lung cancer screening with three-dimensional deep learning on low-dose chest computed tomography," *Nature medicine*, vol. 25, no. 6, pp. 954–961, 2019.
- [13] T. Kooi, G. Litjens, B. Van Ginneken, A. Gubern-Mérida, C. I. Sánchez, R. Mann, A. den Heeten, and N. Karsssemeijer, "Large scale deep learning for computer aided detection of mammographic lesions," *Medical image analysis*, vol. 35, pp. 303–312, 2017.
- [14] J. Needham, *Science and Civilisation in China: Volume 3, Mathematics and the Sciences of the Heavens and the Earth*. Cambridge University Press, 1959, vol. 3.
- [15] C. De Boor, "Bicubic spline interpolation," *Journal of mathematics and physics*, vol. 41, no. 1-4, pp. 212–218, 1962.
- [16] J. Hao, J. Liu, E. Pereira, R. Liu, J. Zhang, Y. Zhang, K. Yan, Y. Gong, J. Zheng, J. Zhang *et al.*, "Uncertainty-guided graph attention network for parapneumonic effusion diagnosis," *Medical Image Analysis*, vol. 75, p. 102217, 2022.
- [17] D. D. Lewis and J. Catlett, "Heterogeneous uncertainty sampling for supervised learning," in *Machine learning proceedings 1994*. Elsevier, 1994, pp. 148–156.
- [18] K. Wang, D. Zhang, Y. Li, R. Zhang, and L. Lin, "Cost-effective active learning for deep image classification," *IEEE Transactions on Circuits and Systems for Video Technology*, vol. 27, no. 12, pp. 2591–2600, 2016.
- [19] A. J. Joshi, F. Porikli, and N. Papanikolopoulos, "Multi-class active learning for image classification," in *2009 IEEE conference on computer vision and pattern recognition*. IEEE, 2009, pp. 2372–2379.
- [20] W. Luo, A. Schwing, and R. Urtasun, "Latent structured active learning," *Advances in Neural Information Processing Systems*, vol. 26, 2013.
- [21] C. E. Shannon, "A mathematical theory of communication," *ACM SIGMOBILE mobile computing and communications review*, vol. 5, no. 1, pp. 3–55, 2001.
- [22] S. Tong and D. Koller, "Support vector machine active learning with applications to text classification," *Journal of machine learning research*, vol. 2, no. Nov, pp. 45–66, 2001.
- [23] S. Huang, T. Wang, H. Xiong, J. Huan, and D. Dou, "Semi-supervised active learning with temporal output discrepancy," in *Proceedings of the IEEE/CVF International Conference on Computer Vision*, 2021, pp. 3447–3456.
- [24] D. Yoo and I. S. Kweon, "Learning loss for active learning," in *Proceedings of the IEEE/CVF conference on computer vision and pattern recognition*, 2019, pp. 93–102.
- [25] A. Freytag, E. Rodner, and J. Denzler, "Selecting influential examples: Active learning with expected model output changes," in *Computer Vision—ECCV 2014: 13th European Conference, Zurich, Switzerland, September 6–12, 2014, Proceedings, Part IV 13*. Springer, 2014, pp. 562–577.
- [26] Z. Liu, H. Ding, H. Zhong, W. Li, J. Dai, and C. He, "Influence selection for active learning," in *Proceedings of the IEEE/CVF International Conference on Computer Vision*, 2021, pp. 9274–9283.
- [27] J. W. Cho, D.-J. Kim, Y. Jung, and I. S. Kweon, "Mcdal: Maximum classifier discrepancy for active learning," *IEEE transactions on neural networks and learning systems*, 2022.
- [28] Z. Wang, Z. Wu, D. Agarwal, and J. Sun, "Medclip: Contrastive learning from unpaired medical images and text," in *Proceedings of the 2022 Conference on Empirical Methods in Natural Language Processing*, 2022, pp. 3876–3887.
- [29] Y. Xie, H. Lu, J. Yan, X. Yang, M. Tomizuka, and W. Zhan, "Active finetuning: Exploiting annotation budget in the pretraining-finetuning paradigm," in *Proceedings of the IEEE/CVF Conference on Computer Vision and Pattern Recognition*, 2023, pp. 23 715–23 724.
- [30] X. Wang, L. Lian, and S. X. Yu, "Unsupervised selective labeling for more effective semi-supervised learning," in *European Conference on Computer Vision*. Springer, 2022, pp. 427–445.
- [31] Q. Shao, J. Kang, Q. Chen, Z. Li, H. Xu, Y. Cao, J. Liang, and J. Wu, "Enhancing semi-supervised learning via representative and diverse sample selection," *arXiv preprint arXiv:2409.11653*, 2024.
- [32] E. W. Forgy, "Cluster analysis of multivariate data: efficiency versus interpretability of classifications," *biometrics*, vol. 21, pp. 768–769, 1965.
- [33] S. Lloyd, "Least squares quantization in pcm," *IEEE transactions on information theory*, vol. 28, no. 2, pp. 129–137, 1982.
- [34] H.-P. Kriegel, E. Schubert, and A. Zimek, "The (black) art of runtime evaluation: Are we comparing algorithms or implementations?" *Knowledge and Information Systems*, vol. 52, pp. 341–378, 2017.
- [35] G. J. McLachlan and T. Krishnan, *The EM algorithm and extensions*. John Wiley & Sons, 2007.

- [36] J. Orava, “K-nearest neighbour kernel density estimation, the choice of optimal k,” *Tatra Mountains Mathematical Publications*, vol. 50, no. 1, pp. 39–50, 2011.
- [37] S. Laine and T. Aila, “Temporal ensembling for semi-supervised learning,” in *International Conference on Learning Representations*, 2016.
- [38] K. He, X. Zhang, S. Ren, and J. Sun, “Deep residual learning for image recognition,” in *Proceedings of the IEEE conference on computer vision and pattern recognition*, 2016, pp. 770–778.
- [39] A. Vaswani, N. Shazeer, N. Parmar, J. Uszkoreit, L. Jones, A. N. Gomez, Ł. Kaiser, and I. Polosukhin, “Attention is all you need,” *Advances in neural information processing systems*, vol. 30, 2017.
- [40] K. Zhang, X. Liu, J. Shen, Z. Li, Y. Sang, X. Wu, Y. Zha, W. Liang, C. Wang, K. Wang *et al.*, “Clinically applicable ai system for accurate diagnosis, quantitative measurements, and prognosis of covid-19 pneumonia using computed tomography,” *Cell*, vol. 181, no. 6, pp. 1423–1433, 2020.
- [41] P. Li, S. Wang, T. Li, J. Lu, Y. HuangFu, and D. Wang, “A large-scale ct and pet/ct dataset for lung cancer diagnosis (lung-pet-ct-dx),” *Cancer Imaging Arch.*, 2020.
- [42] K. Clark, B. Vendt, K. Smith, J. Freymann, J. Kirby, P. Koppel, S. Moore, S. Phillips, D. Maffitt, M. Pringle *et al.*, “The cancer imaging archive (tcia): maintaining and operating a public information repository,” *Journal of digital imaging*, vol. 26, pp. 1045–1057, 2013.
- [43] H. Fan, T. Murrell, H. Wang, K. V. Alwala, Y. Li, Y. Li, B. Xiong, N. Ravi, M. Li, H. Yang, J. Malik, R. Girshick, M. Feiszli, A. Adcock, W.-Y. Lo, and C. Feichtenhofer, “PyTorchVideo: A deep learning library for video understanding,” in *Proceedings of the 29th ACM International Conference on Multimedia*, 2021, <https://pytorchvideo.org/>.